

View Article Online
View Journal

Journal of Materials Chemistry A

Materials for energy and sustainability

Accepted Manuscript

This article can be cited before page numbers have been issued, to do this please use: H. Chen, P. Bal and O. Clemens, *J. Mater. Chem. A*, 2025, DOI: 10.1039/D5TA06611E.



This is an Accepted Manuscript, which has been through the Royal Society of Chemistry peer review process and has been accepted for publication.

Accepted Manuscripts are published online shortly after acceptance, before technical editing, formatting and proof reading. Using this free service, authors can make their results available to the community, in citable form, before we publish the edited article. We will replace this Accepted Manuscript with the edited and formatted Advance Article as soon as it is available.

You can find more information about Accepted Manuscripts in the <u>Information for Authors</u>.

Please note that technical editing may introduce minor changes to the text and/or graphics, which may alter content. The journal's standard <u>Terms & Conditions</u> and the <u>Ethical guidelines</u> still apply. In no event shall the Royal Society of Chemistry be held responsible for any errors or omissions in this Accepted Manuscript or any consequences arising from the use of any information it contains.



3 4

Complex Influence of Stack Pressure on BiF₃ Cathode Materials in All-Solid-State Fluoride-Ion Batteries

- 5 Hong Chen^a, Pervin Bal^a, Oliver Clemens^{a,*}
- 6 a University of Stuttgart, Institute for Materials Science, Materials Synthesis Group,
- 7 Heisenbergstraße 3, 70569 Germany
- 8 * Corresponding Author:
- 9 Prof. Dr. Oliver Clemens
- 10 Email: <u>oliver.clemens@imw.uni-stuttgart.de</u>
- 11 Fax: +49 711 685 51933

15

16

17

18

19

20

21

22

23

24

25

26

27

28

29

30

31

32

33

13 Abstract View Article Online DOI: 10.1039/D5TA06611E

Among all the alternative battery systems beyond lithium-ion batteries (LIBs), all-solid-state fluoride ion batteries (ASSFIBs) are particularly promising due to their high theoretical energy density, thermal stability, and recent advancements in room-temperature superionic solid electrolytes and intercalation-type electrodes. However, their practical application is hindered by poor cycling stability and limited rate capability, largely attributed to unfavored kinetics and interfacial degradation, especially in conversion-type cathodes. Previous studies have shown that the application of stack pressure can significantly improve the cell's cycling stability. To reveal the underlying mechanism, this study systematically investigates the impact of stack pressure on the electrochemical performance of ASSFIBs using BiF₃|BaSnF₄|Sn cells. Among the tested conditions, the best enhancement of cycling stability and rate performance were demonstrated under 180 MPa. Furthermore, ex-situ diffraction analysis revealed pressuredependent phase evolution and oxygen-related interfacial degradation (i.e., BiOF or BiO_{0.1}F_{2.8} formation) in the BiF₃ cathode during the first cycle. Through in-situ electrochemical impedance spectroscopy combined with distribution of relaxation times analysis we identified charge transfer and F⁻ diffusion as the dominant state-of-charge dependent kinetic limitations, with strong correlation to phase transitions within the BiF₃ cathode composite. These findings emphasize the critical role of stack pressure in mitigating interfacial degradation and optimizing ion transport, providing valuable insights for the design and operation of high-performance ASSFIBs.

Keywords

- 34 All solid-state fluoride ion batteries; Conversion-based cathode; Stack pressure; Impedance
- 35 Spectroscopy; Distribution of relaxation times

View Article Online

DOI: 10.1039/D5TA06611E

1 Introduction

The widespread adoption of Li-ion batteries (LIBs) in transportation devices and renewable energy storage systems has reshaped society over the last decades and promises a sustainable future. However, the flammability of liquid electrolytes and the high cost of critical raw materials for LIBs have motivated a technological shift towards all-solid-state batteries (ASSBs) and systems employing alternative shuttle ions, such as Na⁺, Mg²⁺, Cl⁻ and F⁻, to meet ever-increasing demands of large-scale energy storage. Recently, all solid-state fluoride-ion batteries (ASSFIBs) are becoming more competitive due to their high theoretical energy density up to ~5000 Wh L⁻¹using metal fluorides as electrodes^{1, 2}, thermal stability, as well as progress in developing superionic solid electrolytes at room-temperature and intercalation-based electrode materials such as La₂CoO₄, La₂NiO₄, La_{2-x}Sr_xMnO₄ and their derivatives³⁻⁷.

However, in practical application, the potential of ASSFIBs is hindered by poor cycling stability, limited rate capability, unfavored diffusion and/or reaction kinetics, and interfacial degradation.

However, in practical application, the potential of ASSFIBs is hindered by poor cycling stability, limited rate capability, unfavored diffusion and/or reaction kinetics, and interfacial degradation. These limitations can be broadly attributed to two key processes: mechanical inter-particle contact loss (suddenly or progressively) and the chemical decomposition at the interfaces^{8, 9}. Unlike liquid electrolyte systems, where mechanical accommodation occurs more easily, all-solid-state batteries (ASSBs) are subjected to mechanical constraints, from fabrication to operation. Even minor volume fluctuations in active materials can bring substantial internal stress into the system¹⁰. In ASSFIBs, particularly for conversion-based cathode materials, the reduction of metal fluorides (can be described by $MF_y + ye^- \rightarrow M + yF^-$) accompanied by large volumetric changes ($\Delta V \approx 30$ -70 %), will lead to severe delamination between particles within the composite. This can result in poor electronic/ionic percolation, increased overpotential, and ultimately, rapid capacity fading. Furthermore, interface instability between the electrode and solid electrolyte appears to dominate the cell performance in ASSBs, even more than in conventional lithium-ion batteries (LIBs), since the undesirable reaction products cannot

dissolve and diffuse in the solid electrolyte¹¹.

64

65

66

67

68

69

70

71

72

73

74

75

76

77

78

79

80

81

82

83

84

85

86

87

88

89

To overcome these challenges, many strategies have been explored, including viethecte Online DOI: 10.1039/D5TA06611E optimization of electrode composite, and interfacial engineering¹²⁻¹⁷. Among them, applying stack pressure has shown significant benefits by mitigating the inter-particle contact loss and partially stabilizing interfacial reactions¹⁸⁻²³. The effects of stack pressure appear to be systemspecific, depending on the chemical & mechanical properties of the electrode solid electrolyte interface. In all-solid-state lithium-ion batteries (ASSLIBs), numerous studies have shown the pressure-dependent improvement originates from various mechanisms. For example, the ionic conductivity of Li₃InCl₆ increases from 0.35 to 0.52 mS cm⁻¹ when pressure is raised from 2 to 10 MPa at 30 °C, which in turn enhances the utilization of cathode active materials such as single-crystal LiNi_{0.83}Mn0_{.06}Co_{0.11}O₂, leading to 93 % capacity retention after 50 cycles at 10 MPa, compared to 65 % at 2 MPa²¹. Many works have also reported that the intrinsic volume change of electrode active materials determines the critical stack pressure to maintain an intimate and effective interface to achieve sustained cycling. For instance, Silicon anodes (up to 300 % volume expansion upon lithiation) require a stack pressure of 50-120 MPa^{24, 25}, while Nb₂O₅ with 4 % expansion, only needs a minimum stack pressure of 2 MPa to reach capacity retention above 96 % over 30 cycles²². In contrast, zero-strain cathode like Li₄Ti₅O₁₂ (LTO) can maintain coulombic efficiency above 99 % under a minimal pressure of 0.1 MPa²². Our previous study extensively investigated the pressure-dependent conductivity of various solid electrolytes for ASSFIBs and demonstrated significant improvements in electrochemical performance for conversion-based and intercalation-based electrodes under applied stack pressure¹⁸. However, the mechanism underlying the effects of stacking pressure on ASSFIBs remains unexplored. In solid-state batteries, electrode-electrolyte interfacial degradation has been studied using techniques such as XPS, TOF-SIMS, and TEM. Alongside these methods, electrochemical impedance spectroscopy (EIS) has significant advantages as a nondestructive tool for probing interfacial kinetics under operando conditions. While equivalent circuit modelling (ECM) of impedance spectra has traditionally been used for data interpretation, its application in ASSBs is limited by overlapping impedance features with

91

92

93

94

95

96

97

98

99

106

107

108

109

110

111

112

113

114

115

similar time constants and difficulty in distinguishing electrode contributions. In recent yearsticle Online DOI: 10.1039/D5TA06611E distribution of relaxation times (DRT) analysis has been extensively applied in LIBs research²⁶-30, and its application is becoming increasingly important in ASSBs. By converting impedance data into the time domain without circuit assumptions, DRT can reveal distinct relaxation processes, such as charge transfer, ion diffusion, and interphase formation, with high resolution, enabling clearer interpretation of complex interfacial phenomena.

In this work, we report on the pressure-dependent cell performance of a BiF3 cathode composite. The first-cycle performance under varying pressure is investigated, in addition to determining cycling stability and C-rate capability under high stacking pressure. Furthermore, operando X-ray diffraction (XRD) and ex-situ XRD analysis are used to investigate the phase evolution of the BiF₃ cathode in BiF₃|BaSnF₄|Sn cells. In addition, in-situ EIS with DRT analysis is employed to study the state-of-charge (SOC) and pressure dependence of different polarization processes, including charge transfer and ion diffusion. The results reveal the complex multi-scale effects of stack pressure, from crystalline phases formation and O2-/Fdiffusion to macroscopic interfacial behavior, which then collectively influence the overall cell performance.

Experimental

2.1 Material synthesis

Barium fluoride (BaF₂) (99.99 %) and tin fluoride (SnF₂) (99 %) from Sigma Aldrich were used for synthesizing electrolyte BaSnF₄ by mechanical milling and post soft annealing. All starting materials were dried in a vacuum furnace inside an argon-filled glovebox to remove any absorbed moisture. Stoichiometric amounts (~3 g in total) were sealed in a ZrO2 milling vial (50 mL) with ZrO₂ milling balls (5 mm diameter, ball-to-powder ratio of 17:1) under argon atmosphere in the glovebox and milled at 600 rpm for 4 hrs using a Retsch Planetary Ball Mill PM100. After ball milling, the powder mixture was annealed at 300 °C for 2 hrs under dynamic vacuum (10⁻² mbar) using a Büchi Glass Oven B-585. The mechanical milling and the

annealing process were repeated three times to enhance the doping process. Bismuthicle Online Trifluoride (BiF₃) (99 %), Sn nanopowder (>99 %, <150 nm particle size (SEM)) and carbon nanofibers (CNF) (>98 %) from Sigma Aldrich were used to prepare the BiF₃ cathode and Sn anode composites, as described by Reddy et al.³¹. The cathode composite consisted of 40 wt% BiF₃, 50 wt% BaSnF₄, and 10 wt% CNF, while the anode composite contained 50 wt% Sn, 40 wt% BaSnF₄, and 10 wt% CNF. Again, BiF₃ and CNF were dried at 190 °C under dynamic vacuum for 24 hrs using the vacuum furnace before the synthesis process.

2.2 Cell assembly and Electrochemical measurements

Cell pellets were prepared in a three-layers configuration by uniaxial pressing anode composite, electrolyte, and cathode composite using a Specac Atlas 25T manual hydraulic press in an argon-filled glovebox (2 t for 90 s). The mass loadings of electrolyte, anode composite and cathode composite were 200 mg, 10 mg and 5 mg, respectively, i. e., the anode composite was used in excess as compared to the cathode composite. The galvanostatic cycling was performed at 100 °C in the potential range from 0.05 to 1 V (vs. Sn/SnF2) with a current density of 20 µA cm⁻² (unless specified otherwise) on potentiostats from Biologic Science Instruments (VSP or VMP-300 for cycling and VSP-300 for operando XRD measurements). The specific capacities were calculated based on the weight of active material in the cathode composite (BiF3). For the C-rate capability test, a staircase increase of the C-rate (0.02C, 0.5C, 0.1C, 1C) was selected and conducted for three cycles each, after 15 consecutive cycles at 0.01C.

For galvanostatic cycling under different stack pressures, cells were assembled and tested directly in the customized hot-press setup¹⁸. The disc springs were used to minimize the force changes due to dynamic volume change of the pellet during cycling. Stack pressure variation between 20 and 450 MPa were studied due to the stable pressure range of the disc springs used. The chosen electrolyte was first filled in and compacted by hand. Afterwards the anode composite was hand-compacted on one side of the electrolyte and the cathode composite on the other side. The cells were compacted at 450 MPa for 90 s in a housing module made of

144

145

146

147

148

149

150

151

152

153

154

155

156

157

158

159

160

161

162

163

164

165

166

167

168

Al₂O₃ (inner diameter 7.5 mm, corresponding to a cell area of 0.441 cm²) which then sits in side cle Online a steel mantle for radial constraint of the alumina housing. A pair of cylindric hot working steel pins (AISI H11, 7.5 mm in diameter) were used as the current collector, which were aligned and electronically insulated by additional PTFE tubes. The entire hot-press setup was placed inside an argon-filled glovebox for operation under an inert atmosphere to avoid possible material degradations which can be induced by the presence of humidity and/or oxygen. Before cycling, the cell was heated up to the desired temperature and held for at least 4 hrs to reach thermal equilibrium. A pre-stack pressure which is slightly lower than the desired value was applied on the cell before heating, to minimize internal delamination due to thermal expansion, and the actual stack pressure after thermal equilibration was calculated from the recorded onsite force and adjusted accordingly. Cells cycled in typical high-temperature Swagelok type cells³¹ (~0.2 MPa) are referred to as non-pressure cells within this manuscript. To investigate the phase evolution of BiF3 during charging, operando XRD measurements during galvanostatic cycling were conducted at 100 °C, and a Swagelok-type cell of compact design was used³², where the pressure applied to the cell was estimated to be less than 0.1 MPa. The detailed description of operando XRD measurement can be found in chapter 2.3.

To evaluate the SOC and pressure-dependent interfacial degradation of BiF₃ cathode composite, EIS was performed under various stack pressures using VSP or VMP-300, after 2 hrs of galvanostatic cycling at 40 μ A cm⁻² and the following 2 hrs of rest (open-circuit voltage (OCV) monitoring). Impedance spectra were recorded at open circuit state using a signal amplitude of 10 mV in the frequency range of 1 MHz to 100 mHz. DRT analysis was performed using RelaxIS 3 from *rhd instruments*. The DRT transformation with Gaussian radial basis function (RBF)-based discretization was conducted to deconvolute the complex impedance data. The second derivative of the distribution function was used as the penalty item for all patterns in this work, with a shape factor value of 0.5 and regularization parameter $\lambda = 10^{-7}$. The obtained DRT patterns with multiple peaks were fitted using Gaussian functions to

determine the characteristic time constants and peak areas. More details are described incle Online 170 literature²⁸.

2.3 X-ray diffraction

A Rigaku SmartLab diffractometer with a Cu K $\alpha_{1,2}$ radiation (40 kV, 30-40 mA) and a HyPix-3000 detector was used to characterize the crystal structure of the synthesized electrolyte, cathode and anode composites as well as cell pellets after galvanostatic cycling in Bragg-Brentano geometry.

For ex-situ X-ray diffraction experiments, powder samples or cell pellets released from ceramic modules at different SOC were placed in low background airtight sample holders inside an argon-filled glovebox. X-ray diffraction (XRD) patterns were recorded at room temperature, with an incident slit size of 0.3°. A step size of 0.005° was applied in the 20 range from 10° to 80°, leading to a total measurement time of 2 h 35 min. Since the phase evolution of the cell investigated during discharge has been demonstrated in our previous study³², operando XRD patterns were recorded at 100 °C on a cell pellet (cathode side) at discharged state (predischarged to 0.05 V against Sn/SnF₂) while galvanostatic charging was performed in this work. The 20 range was limited to 21.5°-40.5° with a step size of 0.005° (a scan time of 26 min). To obtain sufficient time-resolved data allowing for both phase analysis and quantification, a loop measurement was programmed to record XRD patterns during the galvanostatic charge process, at 1 hr intervals. More details about the operando measurement can be found in our previous publication³².

Rietveld analysis of the diffraction data was performed using TOPAS V6³³, using a fundamental parameters approach as described in literature⁶, with the instrumental broadening being derived from a reference scan on a NIST standard of LaB₆ (660a). To refine the different crystal structures of BiF₃, Bi, and oxidefluorides, crystallographic information, as reported in literature³⁴⁻³⁷, was used without adjusting the atomic positions, but allowing for the refinement of lattice parameters. The structural model for the orthorhombic modification o'-BiF_{3-x} was derived as described in literature³². To account for angular dependent broadening effects from

197

198

199

200

201

202

203

204

205

206

207

208

209

210

211

212

213

214

215

216

217

218

219

220

221

crystallite size and micro strain in the individual phases, two Voigt functions were used wanter online identical thermal displacement parameter of all atoms of all phases was constrained to minimize quantification errors. Batch Rietveld analyses were performed on operando XRD patterns by a python script which repeat the fitting process with the pre-refined boundary values and constraints carefully set on parameters in Topas V6 software to the group of patterns.

3 Results and Discussions

3.1 Pressure effects on cell performance

3.1.1 Cell performance during the first cycle under various stack pressures

Figure 1 shows the relation between the first-cycle behavior of BiF₃ composite and stack pressures. The dQ/dV plots of the cells under various stack pressures during (dis)charge are summarized in Figure 1a), with detailed features within the selected voltage range demonstrated in Figure 1b-e). It can be seen that the peaks in the dQ/dV curves show strong changes with stack pressure. With an increase in stack pressure from 24 MPa to 221 MPa, the cell overpotential, represented by the difference between redox reaction plateaus during dis(charging), reduces by approximately 50 mV (marked by blue arrow in Figure 1b, d and e)). It is indicated by the peaks corresponding to reduction reaction plateaus in the dQ/dV plots. which shift toward higher values (Figure 1d and e), and the peaks corresponding to oxidation reaction plateaus, which shift to lower values (Figure 1b). However, upon further increasing the pressure to 410 MPa, the overpotential begins to rise again (marked by red arrow in Figure 1b, d and e). The corresponding specific capacities of all cells are plotted in Figure 1f, and the charge-to-discharge capacity ratio was calculated to evaluate the cell efficiency. Both discharge and charge capacity are enhanced with stack pressure up to 221 MPa, and decrease with further increasing the pressure, leading to a consistent increase in coulombic efficiency. This observed behavior in the cell overpotential and the (dis)charge capacity correlates well with the pressure-dependent ionic conductivity of the solid electrolyte BaSnF₄. Figure 1g shows the total resistance (bulk and grain boundary contribution are not distinguishable

223

224

225

226

227

228

229

230

231

232

233

234

235

236

237

238

239

240

241

242

(representative EIS measurement is provided in Figure S 2) of the pure electrolyte (200 mg)cle Online under different pressure conditions obtained by electrochemical impedance measurement, between 14 to 450 MPa, which reflects directly the contribution of the electrolyte layer to the polarization process. The logarithm of the ionic conductivity of BaSnF₄ is plotted as a function of pressure as the inset, where the linear decrease in ionic conductivity of BaSnF4 with pressure explained by the so-called activation volume of the electrolyte, i.e., the intrinsic ionic conduction properties of the electrolyte 18, 38. The increase in the electrolyte resistance at lowpressure range is attributed to loss of contact at the pellet interface with current collectors and within the pellet itself (crack formation due to the elastic recovery of the pellet). Furthermore, the DC polarization measurement of BaSnF4 at 100 °C under varied pressure conditions lacks pressure dependency of its electronic conductivity (which is low in the order of 10-9 S cm⁻¹), which rules out an electronic contribution to the observed conductivity trend (Figure S 3). More details on the pressure effects on BaSnF4 and other solid electrolytes in ASSFIBs are provided in our previous study¹⁸. In SSBs, ion conduction of solid electrolyte and, if applicable, through solid electrolyte interfaces (SEIs), are typically static and SOC-independent processes. Therefore, their contribution can be more easily identified³⁹. A similarly relationship was reported by Gao et al.21 in ASSLIBs, where a strong correlation between ionic conduction of electrolyte and the achievable cell capacity was demonstrated. Consistent with these findings, our results indicate that in ASSFIBs based on a BiF₃ cathode, the effect of stack pressure on cell capacity primarily arises from its influence on the pressure-dependent ionic conduction performance of electrolyte, which is reflected by shifts in redox reaction plateaus.



244

245

246

247

248

249

250

251

252

253

254

255

256

257

258

259

260

261

262

263

264

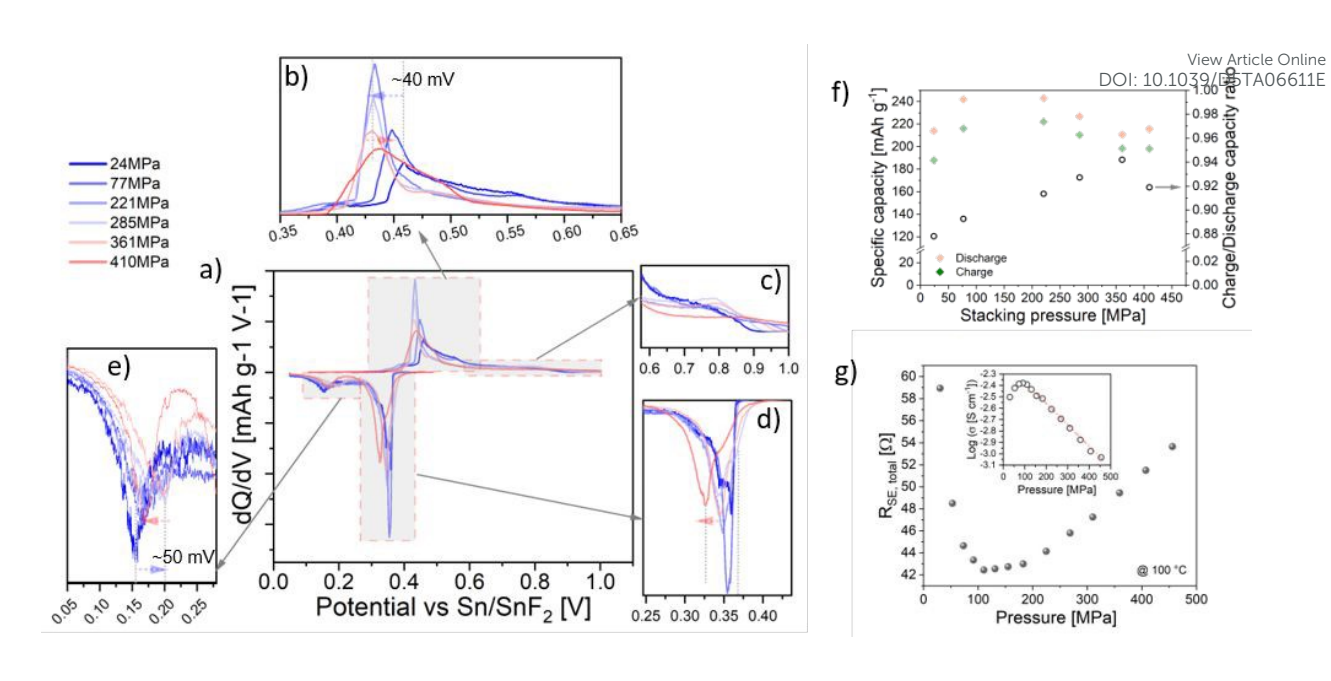


Figure 1 a) dQ/dV plot of the BiF₃|BaSnF₄|Sn cells during first (dis)charge cycle (at 100 °C, current density of 40 uA cm⁻²) under different stacking pressures and selected zoomed features b-e), corresponding potential profiles against capacity is given in Figure S 1; f) pressure dependent specific capacity of (dis)charge process and charge/discharge capacity ratio of the cells in a); g) pressure dependent total resistance of solid electrolyte BaSnF4 at 100 °C; the inset is the logarithm of the corresponding ionic conductivity against pressure.

3.1.2 Cell performance under high stack pressure

To evaluate the long-term impact of stack pressure on the BiF₃|BaSnF₄|Sn cell, galvanostatic cycling was conducted at 100 °C under a constant stack pressure of 180 MPa (selected based on the first-cycle cell performance in 3.1.1) using a current density of 20 µA cm⁻². Our previous study demonstrated that for sufficiently high charge cutoff potential, stack pressure can induce a second plateau around 1.1 V, which could be attributed to side reactions related to fluorination of stainless steel pin or CNF¹⁸. Therefore, in this work, a charge cutoff condition of 1 V was chosen to avoid undesired side reactions. Figure 2a and c) demonstrates the potential profile against capacity of the pressure cell and compares the corresponding coulombic efficiency (CE) and energy efficiency (EE) of both cells. The CE is determined by the ratio of the charge capacity to the discharge capacity from the previous cycle. It can be clearly seen that, in agreement with the findings of our previous study¹⁸, the cell under 180 MPa (Figure 2a) exhibits remarkable stability, retaining a discharge capacity of ~115 mAh g⁻¹ (approximately 50 % of the initial discharge capacity) after 15 cycles, with negligible change in overpotential (i.e., stable flat voltage plateaus). In contrast, the cell under non-pressure condition (see Figure S 4) shows rapid increase in overpotential with cycling, resulting in a drastic capacity fade to Manuscript "Complex Influence of Stack Pressure on BiF3 Cathode Materials in All-Solid-State Fluoride-Ion Batteries"

below 50 mAh g-1 (17 % of the initial value) within just 10 cycles. In Figure 2c), the cell understanding

265

266

267

268

269

270

271

272

273

274

275

276

277

278

279

280

281

282

283

284

285

high stack pressure maintains a CE above 98 % over 150 cycles and exhibits an EE improvement of a factor of approximately 1.5 compared to the non-pressure cell. This pronounced performance enhancement can be attributed to the mitigation of interfacial degradation mechanisms in the pressurized system. In ASSFIBs, large volume change during the conversion reaction, in this case BiF₃ + 3 e⁻ \rightarrow Bi + 3 F⁻ (\triangle V = 29-40 %, depending on the modification of BiF₃),^{37, 40, 41} can induce mechanical delamination at the solid-solid interfaces. leading to sudden or progressive loss of contact, increased impedance and inaccessibility of cathode active material. Our previous study¹⁸ reported that high stack pressure significantly helps to improve the cell's mechanical integrity, which mitigates contact loss between solidsolid particles and preserves electronic and ionic percolation pathway, thereby ensuring sustained access to electrochemically active BiF₃ particles throughout cycling. The comparison of the cross-section SEM images of BiF₃|BaSnF₄|Sn cells after cycling with no pressure and 180 MPa are provided in Figure S 5. Furthermore, Figure 2b and d) demonstrate the C-rate capability of the cell under a stack pressure of 180 MPa. While the internal resistance (IR) drop increases with current density as expected, additional kinetic limitations appear to influence capacity retention. Notably, the observed capacity decay with increasing current density is mostly reversible upon returning to low currents. This effect is particularly more pronounced during charging and becomes more evident in the later stages of charge at high C-rates. indicating the presence of SOC-dependent processes, such as dynamic phase evolution, solid interphases from interfacial degradation at electrode-electrolyte interface.

288

289

290

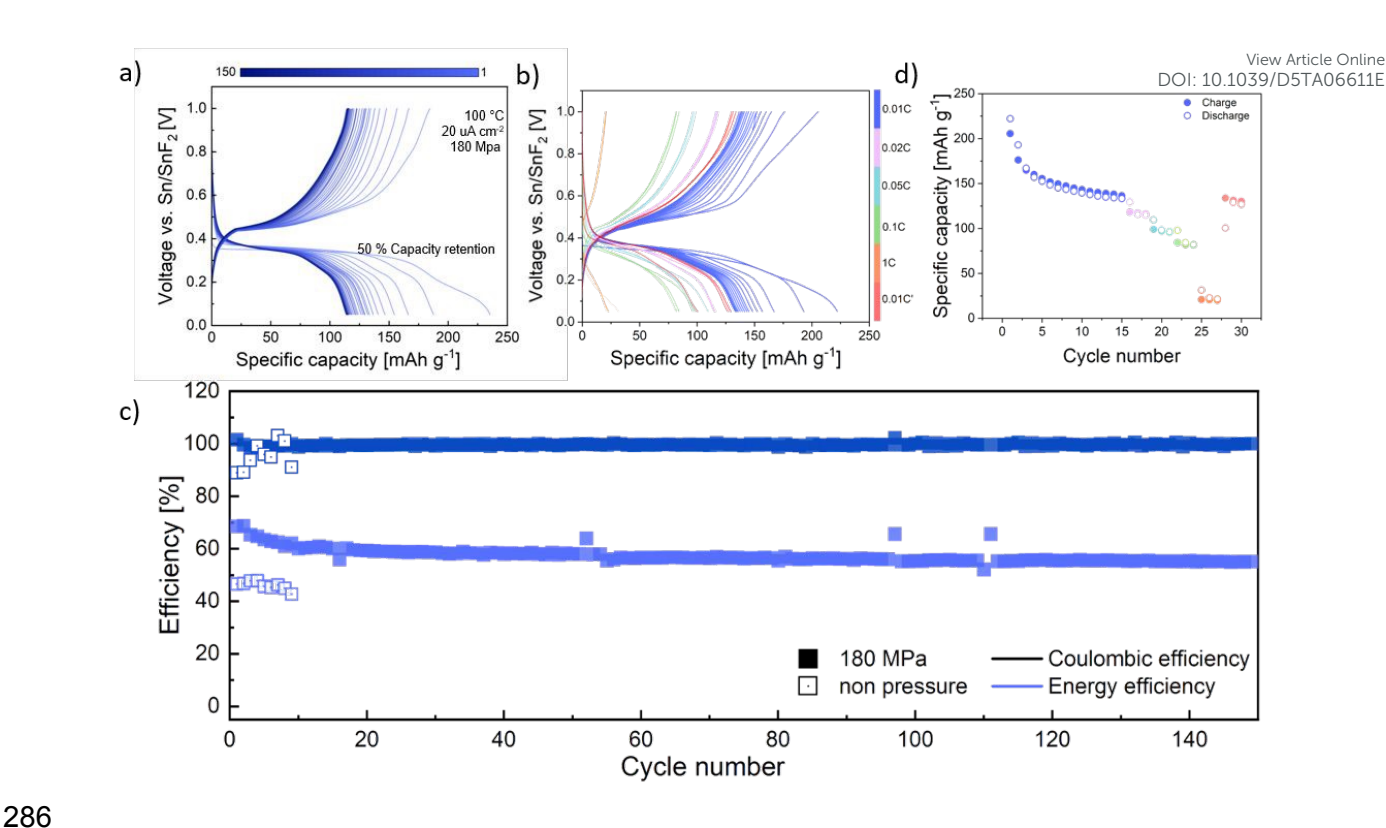


Figure 2 The (dis)charge profiles of the cells cycled at 20 μ A cm⁻² under 180 MPa stack pressure in hot-press set up a) and c) corresponding Coulombic and Energy efficiency; b) Selected C-rate test of the cell under stack pressure of 180 MPa at 100 °C and the corresponding capacity retention d). The 0.01C′ is referred to as the measurements at 0.01C after cycling at 1C (302 mA g⁻¹).

293

294

295

296

297

298

299

300

301

302

303

304

291

3.2 Oxidefluoride formation under different stack pressures

View Article Online DOI: 10.1039/D5TA06611E

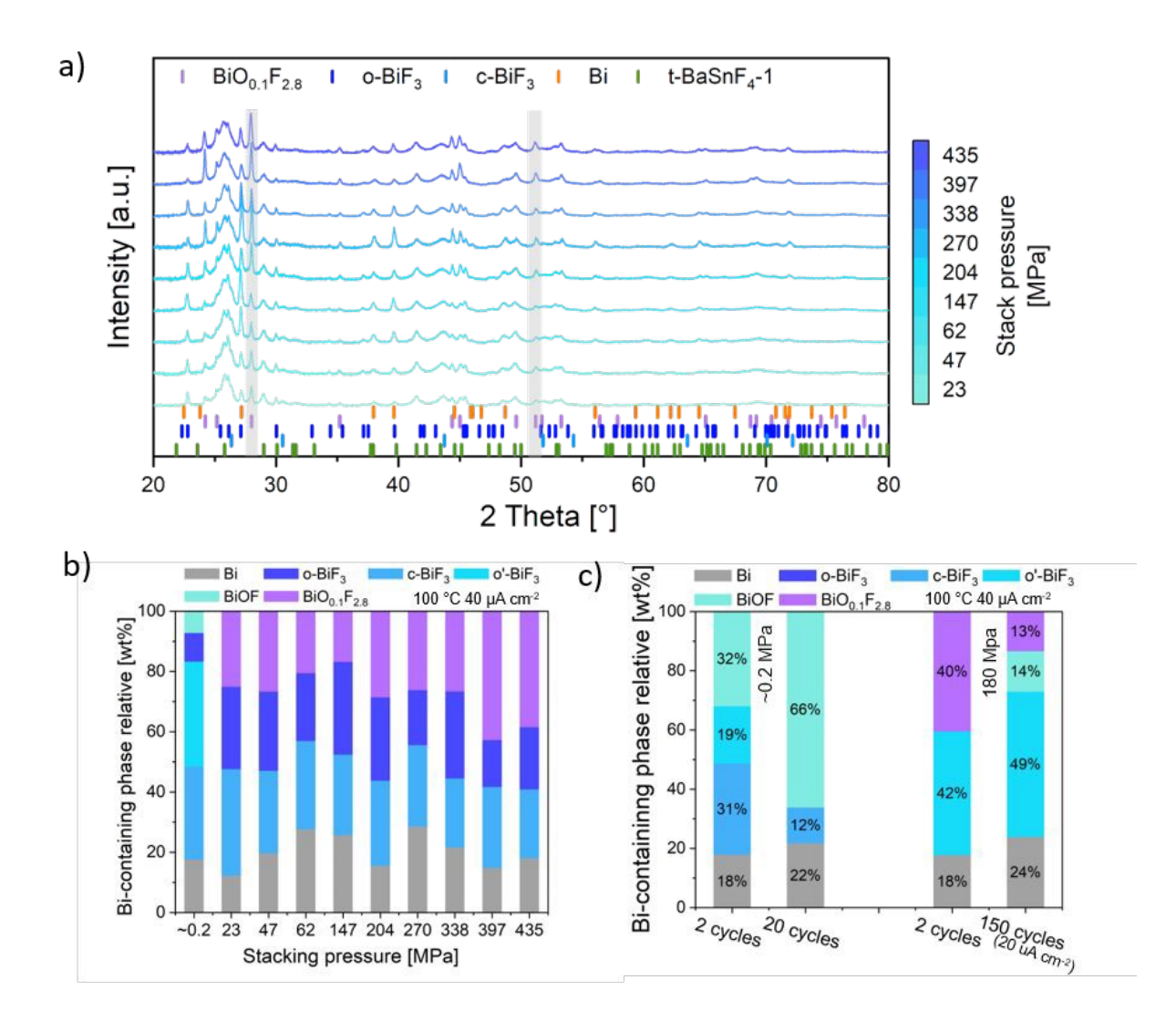


Figure 3 a) Comparison of XRD patterns of the cells cycled at 100 °C with 40 uA cm⁻² under different stacking pressures for 1 cycle (charged to 1 V). Reflections marked by grey rectangles correspond to $BiF_{0.1}O_{2.8}$ (1 0 1) and (2 -1 2); b) Phase analysis on the cells in a), with comparison of non-pressure cell; c) Phase analysis on the cells cycled at 100 °C with 40 uA cm⁻² (20 uA cm⁻² for the 150-cycled cell) for 2 cycles and long-term cycle. Corresponding partial fits are given in Figure S 7 and Figure S 10.

As previously reported³², BiF₃ cathodes undergo a complex phase evolution during discharge at 100 °C, transitioning sequentially from orthorhombic BiF₃ (o-BiF₃) to cubic BiF₃ (c-BiF_{3-x}) and then to a defect-rich orthorhombic phase (o´-BiF_{3-\delta}), before forming metallic Bi. To further investigate the reversibility of this process, operando X-ray diffraction (XRD) was performed on the BiF₃|BaSnF₄|Sn cell upon charging, using identical temperature and current conditions. As shown in Figure S 6), operando XRD reveals partial reversibility of BiF₃ and the detrimental role of the oxidefluoride formation during discharge. Starting from the discharged state (cell

306

307

308

309

310

311

312

This article is licensed under a Creative Commons Attribution 3.0 Unported Licence. Open Access Article. Published on 20 nuvembre 2025. Downloaded on 21/11/2025 21:53:44. 313 314 315 316 317 318 319 320 321

322

323

324

325

326

327

328

329

330

331

potential of 0.05 V), the metallic Bi ($R\overline{3}m$) fluorinated following the reverse pathways to cle Online DOI: 10.1039/D5TA06611E discharging, initially forming o'-BiF_{3-δ} (*Fmmm*), followed by c-BiF_{3-x} (*Fm*3̄*m*), with increasing F⁻ insertion into the lattice. This process is evidenced by the coherent increase in weight fraction of both phases observed. However, the oxidefluoride BiOF (P4/nmm) formed during discharging was found to be electrochemically inactive once formed and persists throughout the charging process. This is attributed to the thermodynamically stable nature of the Bi-O bond under cell operating conditions (100 °C), which makes F-/O2- exchanging highly unfavorable. Also, oxygen diffusion is sluggish at solid-solid interfaces compared to fluoride ion diffusion, further limiting the reversibility³². Furthermore, when the cell is charged to 1 V, no orthorhombic BiF₃ (Pnma) was observed, and the cell volume of the formed c-BiF_{3-x} (~195.9(2) Å³) is smaller as compared to the initial value (~199.2(2) Å³)) observed before the first discharge process³². This likely indicates a defect-richer structure and plausible oxygen incorporation in cubic phase during charge⁴².

To understand the effects of stack pressure on the phase evolution, ex-situ XRD was conducted on cells charged to 1 V after cycling under various stack pressures. Figure 3a) compares the ex-situ XRD patterns of those cells, and it can be seen, from the reflections marked by grey rectangles in Figure 3a), that the phase evolution of BiF_{0.1}O_{2.8} in the BiF₃ cathode exhibits pressure-dependent behavior. As a result obtained from detailed Rietveld analysis, the relative weight fraction of Bi-containing phases in BiF3 cathode composite is shown in Figure 3b) (Partial fits are given in Figure S 7 and Figure S 10). In contrast to nonpressure conditions, even when only a moderate pressure of 20 MPa is applied, BiOF can no longer be detected; instead a F-rich oxidefluoride BiO_{0.1}F_{2.8} phase³⁵ (P6₃/nmm, a=4.083 Å. c=7.323 Å), is observed. This phase is structurally and chemically distinct to orthorhombic³⁷ and cubic BiF₃ modifications³² and BiOF³⁵ (P4/nmm, a=3.746(9) Å. c=6.226(1) Å), but has a very similar powder XRD pattern to trigonal BiF₃⁴³ ($P\overline{3}c$, a=7.165 Å. c=7.318 Å). However, there is a very strong difference in the unit cell volumes that have been observed for those phases. As an example, the overview of crystallographic data of BiF3 and oxyfluorides obtained in the

333

334

335

336

337

338

339

340

341

342

343

344

345

346

347

348

349

350

351

352

353

354

355

356

357

358

partial fit of BiF₃ cathode composite of a cell pellet (dis-)charged (0.05-1 V) under a pressure cle Online DOI: 10.1039/D5TA06611E of 180 MPa (Figure S 8) is list in Table S 1. The volume per BiO_xF_{3-2x} (0≤x≤1) unit in trigonal BiF₃ and the compound observed by us is very different by ~ 2.6 %, whereas the orthorhombic modification observed fits with the volume within errors (~ -0.07 % volume difference to what has been reported in literature³⁷), and the smaller difference of the cubic modification is explained by its defect richer nature (as outlined in detail in our previous article³²). A volume difference of 2.6 % for a symmetry distorted variant must thus have another origin. Given the volume evolution of BiO_xF_{3-2x} on oxygen substitution (Table S 2 and Figure S 9) appears a fairly linear dependence on the oxygen content x in BiO_xF_{3-2x} unit. The lattice parameters and volume we observed are very much in agreement with the reported hexagonal modification of BiO_{0.1}F_{2.8}, giving even a better fit with reduced R_{wp} value (in Table S1). Both, our previous study³² as well as this work have shown that in the pressure-free cells the presence of the tetragonal modification of BiOF (with a very low volume per BiO_xF_{3-2x}) is unquestionable. Since O substitution is thus a known phenomenon to occur within the cathode composite³², the identification of the low-O content bismuth oxyfluoride BiO_{0.1}F_{2.8} with clearly different volume per BiO_xF_{3-2x} unit than trigonal BiF₃ is well conclusive. However, one should be aware that the oxygen content cannot be determined precisely here, but that an overall fluorine-rich composition is indicated. Interestingly, the formation of BiO_{0.1}F_{2.8} is contradictory to the mechanism for the formation of BiOF at the later discharge stage, which involves introduction of F- defects into BiF₃ and accumulation of oxygen impurity during defluorination³². To clarify the origin of BiO_{0.1}F_{2.8}, cells cycled under 20 MPa and 180 MPa were analyzed by ex-situ XRD at discharged state (cell potential of 0.05 V). As shown in Figure S 11, no BiOF or BiO_{0.1}F_{2.8} is detected at the discharged state, suggesting that BiO_{0.1}F_{2.8} most likely forms under pressure in the later stage of charging (considering its fluorine-rich composition). This finding implies that stack pressure affects oxygen transport kinetics in BiF₃ composite, especially, O²- diffusion appears to be suppressed within the investigated pressure range, which are critical for the phase evolution.

360

361

362

363

364

377

378

379

380

381

382

383

384

Notably, the pressure-dependent formation of $BiO_{0.1}F_{2.8}$ appears closely correlated to the Vionical Online DOI: 10.1033/D5TA06611E conductivity trend of BaSnF₄ discussed in Section 3.1. With increasing stack pressure from 20 MPa to 150 MPa (in Figure 3b), a reduced weight fraction of BiO_{0.1}F_{2.8} is observed, with further increase in applied pressure, the amount of BiO_{0.1}F_{2.8} rises again. This observation indicates the formation of BiO_{0.1}F_{2.8} to be a consequence of the interplay between the kinetics of F- and O2- diffusion and their different activation volumes within BiF3 cathode composite, which result in different pressure dependencies of the fluoride and oxide ion transport. Pure fluorides are in general poor oxygen conductors and, to our best knowledge, there is no study on oxygen conduction (and pressure dependency) within BaSnF4 or other fluorides so far. However, many studies on the activation volume for O²⁻ in fluorite-type oxides and F- in fluorite-type (-related) fluorides have been reported^{18, 44}. Christopoulos et al.⁴⁴ reported that the activation volume of O²- diffusion in fluorite structured oxides (ThO₂, UO₂ and PuO₂) at room temperature locate in the range of 10⁻¹⁴ cm³ mol⁻¹. Even for a superior oxide conductor ZrO₂ (doped with 8 mol% Y₂O₃)⁴⁵, the activation volume for O²⁻ transport at 750 °C is 2.08 cm³ mol⁻¹. In our previous study¹⁸, the determined activation volume of F⁻ in BaSnF₄ is 1,01(2) cm³ mol⁻¹ at 30 °C. Given that the activation volume of O²⁻ diffusion is significantly higher than F- diffusion due to its larger ionic radius and higher covalency, our observation of reduced formation of bismuth oxyfluorides under pressure conditions are well in line with this behavior, suggesting that the O²diffusion process is considerably more sensitive towards stack pressure than Fdiffusion within the cathode composite. In addition, by studying low-pressure cells using operando XRD it is confirmed that the O species in the composite contribute to the formation of BiOF during discharging by plausible F-/O2- exchange mechanism at electrode-electrolyte interfaces³². Therefore, under stack pressure the eliminated voids and the improved contact between particles would certainly affect the O²⁻ diffusion at the interfaces. In summary, we interpret the pressure-dependent formation of BiO_{0.1}F_{2.8} as follow:

From 20 MPa to 450 MPa, the solid-solid contact has been improved by increasing pressure to online

385

386

387

388

389

390

391

392

393

394

395

396

397

398

399

400

401

402

403

404

405

406

407

408

409

410

411

and thus reduced the availability of the interfacial pathway for O²⁻ diffusion in the cathode composite, while the F⁻ transport is still dominated by the solid electrolyte. Initially, as the pressure increases from 20 MPa to 150 MPa, the suppression of O²⁻ diffusion combined with enhanced F⁻ transport leads to the reduced formation of BiO_{0.1}F_{2.8}. At pressures beyond 200 MPa, the ionic conductivity of BaSnF₄ significantly drops, limiting F⁻ transport to a level more comparable with O²⁻ diffusion. As a result, the weight fraction of the BiO_{0.1}F_{2.8} phase increases again slightly, possibly indicating a pressure threshold beyond which F⁻ transport becomes a rate-limiting factor for oxyfluoride formation.

It is important to note that oxygen accumulation is a continuous process during cell operation, particularly in the system where the solid electrolyte is the main source of oxygen impurity³². Given that, prolonged cycling would unavoidably lead to an increase of oxidefluoride content. This agrees with the findings reported in Figure 3c), which compares the weight fraction of Bicontaining phases of cells under non-pressure conditions and constant pressure of 180 MPa after cycling. After 20 cycles without stack pressure, BiOF accounts for approximately two thirds of the Bi-containing phases. This finding is consistent with the severely decayed capacity to below 10 % of the theoretical value of 302 mAh q⁻¹. In contrast, under 180 MPa, the oxygen accumulation is significantly suppressed, with prolonged cycling its negative impact becomes pronounced. After 150 cycles, partial transformation of BiO_{0.1}F_{2.8} to BiOF is observed, indicating gradual interfacial degradation. This observation is well reflected in the cell capacity decay observed in Figure 2a), confirming that by applying optimized pressure, the oxygenaccumulation-related degradation can be significantly reduced, but not eliminated. Thus, these results reveal a dual impact of stack pressure, promoting F- diffusion and suppressing O²transport. Nevertheless, the presence of oxygen impurities remains a critical limitation, especially in long-term cycling, even at optimized pressure ranges. This emphasizes the importance of solid electrolyte purity, improved interfacial design and cell fabrication for ASSFIBs.

413

414

415

416

417

429

430

431

432

433

434

435

436

437

438

3.3 *In-situ* EIS-DRT analysis under different stacking pressures

View Article Online DOI: 10.1039/D5TA06611E

As discussed in Section 3.1, the effect of stack pressure on BiF₃ cathode in ASSFIBs is closely related to the pressure-dependent ionic conductivity of BaSnF₄, as reflected by the shift of the flat voltage plateaus. However, cycling performance under pressure also reveals additional, nonnegligible contributions from kinetic limitations, particularly evident at later SOCs and correlating with the observed capacity decay. Such kinetic limitations are primarily attributed to charge transfer and ion diffusion processes within Bi-containing active materials, both of which are typically dynamic processes and SOC-dependent, each with distinct time constants which can be probed by EIS. To further understand these processes, in-situ EIS-DRT analysis was conducted at different OCVs during the first cycle under three pressure conditions as used for the cell characterization: moderate (20 MPa, Figure 4a), high (180 MPa, Figure 4b), and ultra-high (430 MPa, Figure 4c). The evolution of the Impedance spectra during discharge and charge during OCV monitoring is shown in Figure 4a-c next to the corresponding cell potential profiles, respectively. The corresponding DRT patterns are given in Figure 4d-f, indicated with specific time constant regimes. In particular, the SOC-dependent interfacial processes, which could be identified and categorized based on a comparison to literature values of typical kinetics processes in solid-state batteries ^{26, 28} (one example of peak fitting and more comments on categorization are shown in Figure S 12, are plotted against the OCV in Figure 5a-b, and the detailed values are listed in Table S 3 to Table S 14.

As can be seen in Figure 5a-b and the corresponding DRT plots shown Figure 4d-f, the single peak with highest intensity in τ_3 (>1 s) regime is attributed to the ion F⁻ diffusion in the polycrystalline Bi-containing electrode materials (including bulk and grain boundary contributions). The less pronounced peaks located in the faster τ_2 (10⁻²-10⁰ s) regime correspond to the charge-transfer processes of both electrodes. These peaks also reflect the microstructural changes at electrode-electrolyte interfaces with a change of SOCs. In the τ_1 (10⁻⁵-10⁻² s) regime, we assign the smaller peak to the charge transfer across any interphases. In the τ_0 (<10⁻⁵ s) regime, contributions from solid electrolyte (i.e. contributions from both, bulk

and grain boundary responses of the nanocrystalline BaSnF₄ electrolyte, hereafter referred tocle Online as R_{SE}) and the potential contact resistance with the current collector are present. Due to the absence of a semicircle corresponding to BaSnF₄ within the measured frequency range, the R_{SE} was determined by the intercept of Nyquist plots on the real impedance axis and excluded from DRT fitting (Figure S 12). For all three pressure conditions, R_{SE} reveals a nearly constant value during both defluorination and fluorination, indicating SOC independence as would be expected for an electrolyte; the detailed values are listed in Table S 3 to Table S 14.

To confirm the dominance of BiF $_3$ cathode-relate kinetic processes, a control EIS-DRT measurement was performed on a Sn/SnF $_2$ symmetric cell at half fluorination state (Sn to SnF $_2$ mass ratio is 1:1) and after 20 cycles (Figure S 13). It is found that such a Sn anode retains a relatively stable overpotential (slowly growing up to 15 mV over 24 cycles); its contribution to BiF $_3$ |BaSnF $_4$ |Sn cell can thus be considered to be negligible. Furthermore, though the Sn/SnF $_2$ electrode exhibits similar time constants as BiF $_3$ cathode, compared to BiF $_3$, the evolution of the peak's intensity is small and the corresponding resistances are much smaller (Rct is around 20 times lower and Rdiff is 50 times up to 2 magnitudes lower than that of the BiF $_3$ side). Hereby, it is confirmed that the measured kinetics in BiF $_3$ |BaSnF $_4$ |Sn cells predominately reflect the behavior of BiF $_3$ cathode.

464

465

466

467

468

469

470

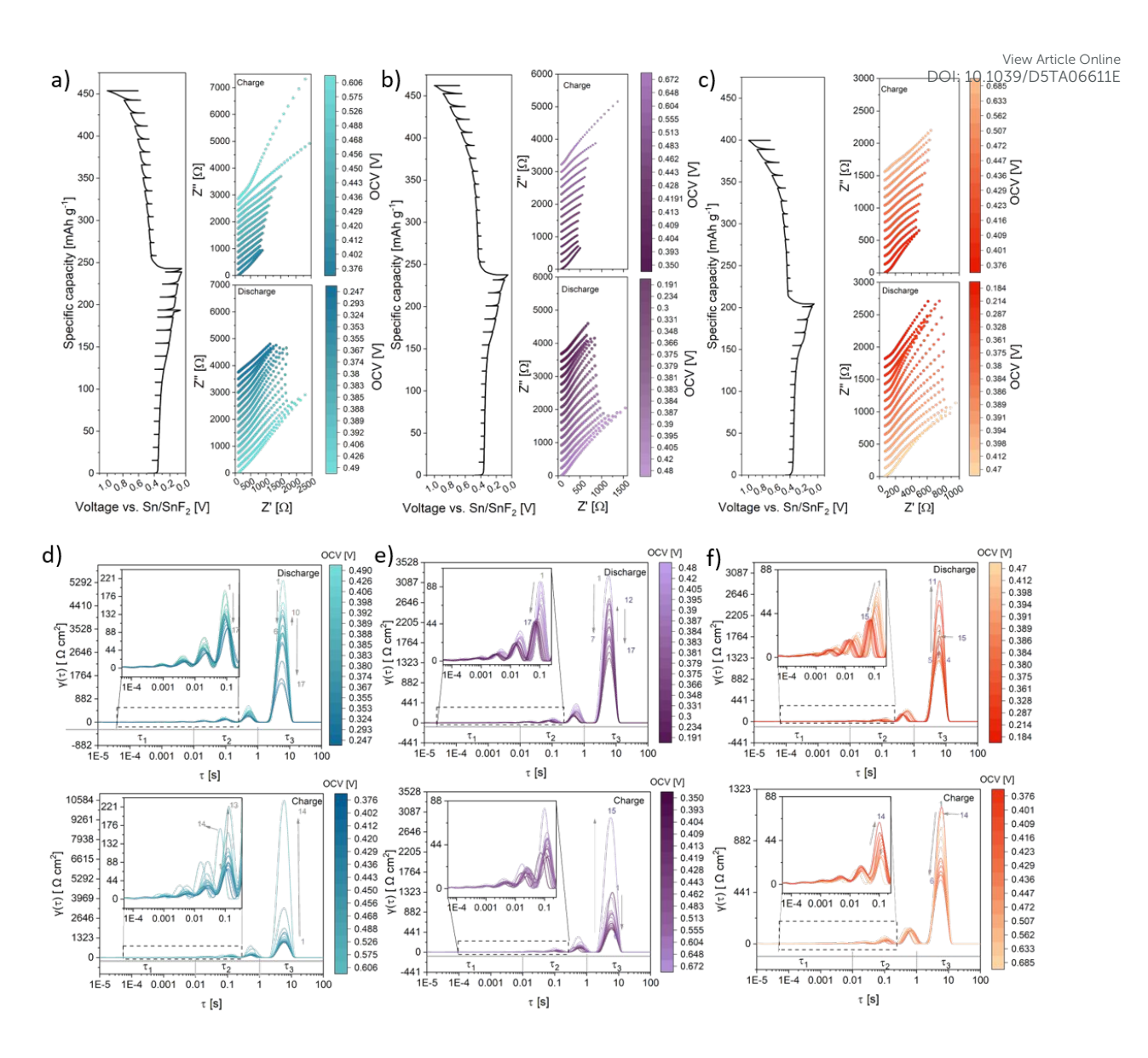


Figure 4 In-situ EIS-DRT analysis of the BiF₃|BaSnF₄|Sn cells under stacking pressures. a) 22 MPa)(left) Voltage profile with selected SOCs and (right) corresponding Nyquist plots during discharge and charge; b) 180 MPa (left) Voltage profile with selected SOCs and (right) corresponding Nyquist plots during discharge and charge; c)430 MPa (left) Voltage profile with selected SOCs and (right) corresponding Nyquist plots during discharge and charge; d-f)Corresponding DRT patterns of the cells in a-c) with specific time constant regimes indicated (SE resistance is determined by the intercept of Nyquist plots at real impedance axis and is not included in DRT analysis due to the absence of a semicircle.)

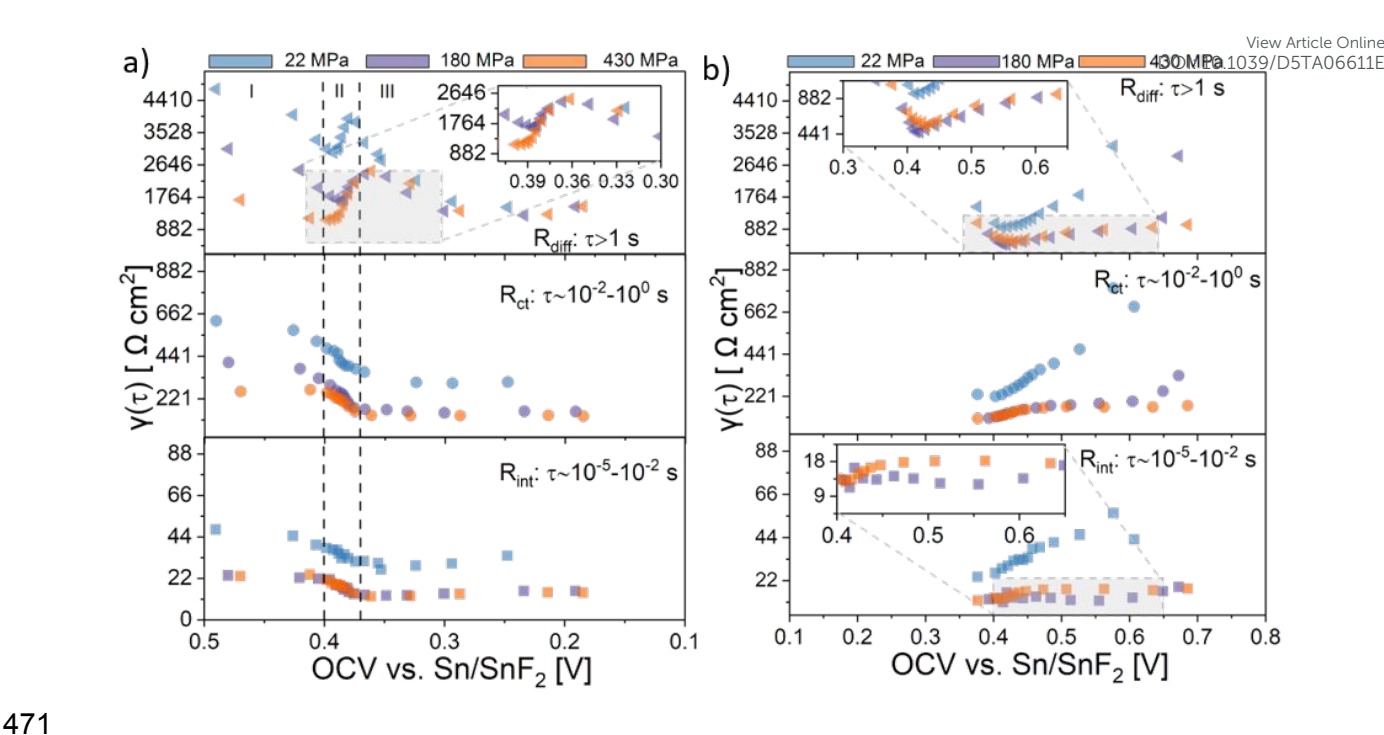


Figure 5 Fitted resistances of the cells in Figure 4a-c) (interphase, charge transfer and diffusion through Bicontaining electrode active materials (CAMs)) are categorized according to their characteristic time constants.

As can be seen in Figure 5a-b, across three pressure conditions, the dominant SOC-dependent processes in the BiF $_3$ cathode composite are charge transfer (resistance referred to as R_{ct}) and ion diffusion processes (R_{diff}). Here F^{-} diffusion is considered to be the primary contribution due to the minor fraction of the oxygen impurity and much slower oxygen accumulation (predominantly along solid-solid interfaces) 32 . Similarly, it has been reported for oxide electrode materials such as $Li_7Ti_5O_{12}$ (LTO) in LIBs that those two processes are kinetically dominant and are sensitive to the SOC. As described in the previous chapter, the formation of oxidefluoride phases (e.g., BiOF and BiO $_{0.1}F_{2.8}$) is generally suppressed under the pressure conditions investigated in this work. Correspondingly, the associated R_{int} remains small during cycling and relatively stable during discharge. However, R_{int} exhibits a pronounced increase during charging, particularly for later SOCs (discussion see later in this chapter). Thus, we conclude that the charge transfer and diffusion processes exhibit relatively high resistance values at the beginning of discharge, which can be attributed to the need for activation process and the low concentration of F^- defects in the fully charged BiF $_3$ lattice, requiring nucleation of the metallic Bi phase. Reversibly, the increase in R_{diff} and R_{ct} at the end of charging results

490

491

492

493

494

495

496

497

498

499

500

501

502

503

504

505

506

507

508

509

510

511

512

513

514

515

from the reduced availability of F^- defects and the poor electronic conductivity of $BiF_3^{46/i}$ and $Cic Online oxidefluorides^{47, 48}$, once present, compared to metallic Bi and CNF.

With increasing stack pressure, R_{diff}, R_{ct} and R_{int} all decrease significantly from moderate (20 MPa) to high pressure (180 MPa), primarily due to drastically improved solid-solid interparticle contact. However, at the highest pressure investigated (430 MPa), only a minor impact of resistance reduction can be observed, though other effects, such as lattice distortion and pressure-induced phase evolution, become dominant under this condition.

Notably, during the first defluorination, R_{diff} shows a complex behavior with two minima, in agreement with three stages of structure evolution as described in our previous study³². With F- extraction and Bi formation, orthorhombic BiF₃ transitions to cubic BiF_{3-x}, then an orthorhombically distorted phase is formed prior to the formation of Bi metal becoming predominant (referred to as Stage I, II and III marked in Figure 5a). It can be clearly seen that: in Stage I Rdiff decreases during the transition from o-BiF3 to c-BiF3, then increase in stage II with the o'-BiF_{3-ō} increases its fraction. Finally, in stage III, R_{diff} decreases when the phase fraction of o'-BiF_{3-ō} decreases again. Considering that F⁻ diffusion within the grain of Bicontaining active materials occurs mainly through a vacancy-exchange mechanism, an increase in F⁻ vacancy concentration would initially enhance the ion mobility. Once the amount of F- defects reaches a certain threshold, the defects tend to cluster, leading to structural distortion, and this appears to increase the resistance for F- within the electrode. This change is observed independent of stack pressure, indicating that this partial defluorination mechanism is intrinsic to BiF₃ cathode. In the subsequent fluorination on charging, R_{diff} only possesses a single minimum observed at OCVs between 0.35 to 0.45 V, coinciding with the formation of o'-BiF_{3-ō} at the beginning of fluorination. R_{diff} then increases again as fluorination proceeds via formation of c-BiF $_{3-x}$ to o'-BiF $_{3-\delta}$, consistent with the reversible phase transformation observed by operando and ex-situ XRD. Noticeably, over stage II to III of defluorination, R_{diff} increases at 430 MPa and even exceed the value under 180 MPa, being even 1.5 times higher than before cycling. Given the defect-richer nature of intermediate o´-BiF_{3-ō} phase in this region, it

532

533

534

535

536

537

538

539

540

541

542

516

517

518

519

520

is plausible that this modification exhibits a distinct activation volume, making the F- mobility of Online more susceptible to pressure effect than in other modifications. This could be considered the most plausible origin for the capacity degradation described in Figure 1b. This is also in agreement with the increased R_{diff} under 430 MPa during charging in the OCV range from 0.35 to 0.5 V. Overall, these findings indicate that, despite enhanced interparticle contact at high stack pressures, which should facilitate charge transport, excessive pressure may instead negatively affect the ion F- mobility within defect-rich phases of the Bi/BiF₃ cathode. We also note that the suppression of F- mobility aligns well with the increased formation of BiO_{0.1}F_{2.8} under pressure beyond 200 MPa (see Section 3.2), likely arising from the competitive F- and O²⁻ diffusion kinetics. This also explains the higher R_{int} observed at 430 MPa compared to 180 MPa (Figure 5b). Overall, the DRT study in combination with diffraction analysis shows that the stack pressure must be carefully optimized to balance between improved interfacial contact and adverse effects on ionic transport and phase stability.

Conclusions

In this work, we systematically investigated the effects of stack pressure on the electrochemical performance, phase evolution and kinetic behavior of BiF₃ cathode in all-solid-state fluorideion batteries (ASSFIBs), using BaSnF4 as the solid electrolyte. By integrating galvanostatic cycling, operando & ex-situ XRD, and in-situ EIS-DRT analysis under varied stack pressures, we revealed a multifaceted pressure-dependent behavior that determines both thermodynamic aspects of phase formation and kinetic processes of ion transport within the cathode composite.

Our results demonstrated that applying high pressures (150-180 MPa) significantly improves cell capacity, coulombic efficiency, and long-term cycling stability. This enhancement is not only attributed to the improved mechanical contact between solid-solid interfaces and the increased ionic conductivity of BaSnF₄, which reduces the cell overpotential and collectively preserves electronic and ionic percolation pathways, but also to the suppression of the formation of oxygen-rich BiOF and corresponding interfacial degradation. In contrast, cells

Open Access Article. Published on 20 nuvembre 2025. Downloaded on 21/11/2025 21:53:44.

This article is licensed under a Creative Commons Attribution 3.0 Unported Licence.

under insufficient pressure suffer from interfacial degradation, including delamination variable online collective oxidefluoride formation (BiOF or BiO_{0.1}F_{2.8}), explaining rapid capacity decay; the XRD result reveals that excessive pressures beyond 200 MPa lead to increased BiO_{0.1}F_{2.8} formation, by suppressing F⁻ mobility and promoting competitive diffusion with oxygen impurities. While optimized stack pressure hinders the oxygen accumulation, the related interfacial degradation due to residual oxygen impurity remains unavoidable during prolonged cycling, emphasizing the critical need for electrolyte purification and interface design.

Through in-situ EIS-DRT analysis, we identified different kinetic processes and correlated to observed phase evolution and capacity decay. It is revealed that charge transfer and ion diffusion within Bi-containing active materials are the dominant SOC-dependent kinetic processes. The resistance contributions R_{diff} and R_{ct} exhibit strong correlation with structure evolution, evidenced by the observed changes of R_{diff} during defluorination and fluorination, respectively, highlighting the intrinsic nature of phase-change-driven F⁻ mobility in BiF₃. Moreover, excessive stack pressure (430 MPa) was found to suppress F⁻ mobility, particularly at defect-rich stages.

Overall, our findings demonstrate that the influence of stack pressure on ASSFIBs is non-monotonic and governed by a complex interplay between mechanical contact, competing ion transport and phase evolution. Careful optimization of stack pressure is essential to balance mechanical stability, ionic transport and phase reversibility, and to ensure the high-performance fluoride-ion battery systems.

5 Conflicts of Interest

There are no conflicts of interest to declare.

6 Author contributions

H.C.: executed the synthesis of the precursors, preparation of the electrochemical cells and samples for further characterization measurements such as *operando* and *ex-situ* XRD and *in-*

- 568 situ EIS measurements, performed ex-situ and operando XRD measurements and in-situ EIScle Online
- measurements, analyzed XRD, EIS(DRT) and GCPL data including plotting of data, wrote the
- 570 manuscript. P.B.: synthesis of the precursors, preparation of the electrochemical cells and
- 571 samples for GCPL measurement under various stack pressures for 1 cycle and conducted
- 572 GCPL measurements for further characterization under the supervision of H.C. O. C.: guided
- and supervised the project, contributed to writing the manuscript.

7 References

- 1. Davis, V. K.; Bates, C. M.; Omichi, K.; Savoie, B. M.; Momčilović, N.; Xu, Q.; Wolf, W. J.; Webb, M. A.; Billings, K. J.; Chou, N. H.; Alayoglu, S.; McKenney, R. K.; Darolles, I. M.; Nair, N. G.; Hightower, A.; Rosenberg, D.; Ahmed, M.; Brooks, C. J.; Miller, T. F.; Grubbs, R. H.; Jones, S. C., Room-temperature cycling of metal fluoride electrodes: Liquid electrolytes for high-energy fluoride ion cells. *Science* **2018**, *362* (6419), 1144-1148.
- 2. Potanin, A. A. Patent 7,722,993 B2. 2010.
- 3. Nowroozi, M. A.; Ivlev, S.; Rohrer, J.; Clemens, O., La₂CoO₄: a new intercalation based cathode material for fluoride ion batteries with improved cycling stability. *Journal of Materials Chemistry A* **2018**, *6* (11), 4658-4669.
- 4. Nowroozi, M. A.; Wissel, K.; Donzelli, M.; Hosseinpourkahvaz, N.; Plana-Ruiz, S.; Kolb, U.; Schoch, R.; Bauer, M.; Malik, A. M.; Rohrer, J.; Ivlev, S.; Kraus, F.; Clemens, O., High cycle life all-solid-state fluoride ion battery with La₂NiO_{4+d} high voltage cathode. *Communications Materials* **2020**, *1*, 27.
- 5. Vanita, V.; Waidha, A. I.; Vasala, S.; Puphal, P.; Schoch, R.; Glatzel, P.; Bauer, M.; Clemens, O., Insights into the first multi-transition-metal containing Ruddlesden–Popper-type cathode for all-solid-state fluoride ion batteries. *Journal of Materials Chemistry A* **2024**, *12* (15), 8769-8784.
- 6. Wissel, K.; Schoch, R.; Vogel, T.; Donzelli, M.; Matveeva, G.; Kolb, U.; Bauer, M.; Slater, P. R.; Clemens, O., Electrochemical Reduction and Oxidation of Ruddlesden–Popper-Type La₂NiO₃F₂ within Fluoride-Ion Batteries. *Chemistry of Materials* **2021**, 33 (2), 499-512.
- 7. Vanita, V.; Mezzadra, G.; Tealdi, C.; Clemens, O., Fluoride Ion Transport and Phase Evolution in the Cathode Material LaSrMnO₄ within All-Solid-State Fluoride Ion Batteries. *ACS Applied Energy Materials* **2025**, *8* (11), 7562-7574.
- 8. Ohta, N.; Takada, K.; Sakaguchi, I.; Zhang, L.; Ma, R.; Fukuda, K.; Osada, M.; Sasaki, T., LiNbO₃-coated LiCoO₂ as cathode material for all solid-state lithium secondary batteries. *Electrochemistry Communications* **2007**, *9* (7), 1486-1490.
- 9. Ohta, N.; Takada, K.; Zhang, L.; Ma, R.; Osada, M.; Sasaki, T., Enhancement of the High-Rate Capability of Solid-State Lithium Batteries by Nanoscale Interfacial Modification. *Advanced Materials* **2006**, *18* (17), 2226-2229.
- 10. Zhang, W.; Schröder, D.; Arlt, T.; Manke, I.; Koerver, R.; Pinedo, R.; Weber, D. A.; Sann, J.; Zeier, W. G.; Janek, J., (Electro)chemical expansion during cycling: monitoring the pressure changes in operating solid-state lithium batteries. *Journal of Materials Chemistry A* **2017**, *5* (20), 9929-9936.
- 11. Koerver, R.; Aygün, I.; Leichtweiß, T.; Dietrich, C.; Zhang, W.; Binder, J. O.; Hartmann, P.; Zeier, W. G.; Janek, J., Capacity Fade in Solid-State Batteries: Interphase Formation and Chemomechanical Processes in Nickel-Rich Layered Oxide Cathodes and Lithium Thiophosphate Solid Electrolytes. *Chemistry of Materials* **2017**, *29* (13), 5574-5582.

- 12. Janek, J.; Zeier, W. G., A solid future for battery development. *Nature Energy* **2016** Affice Online (9), 16141.
- 13. Kato, Y.; Hori, S.; Saito, T.; Suzuki, K.; Hirayama, M.; Mitsui, A.; Yonemura, M.; Iba, H.; Kanno, R., High-power all-solid-state batteries using sulfide superionic conductors. *Nature Energy* **2016**, *1* (4), 16030.
- 14. Zhang, W.; Weber, D. A.; Weigand, H.; Arlt, T.; Manke, I.; Schröder, D.; Koerver, R.; Leichtweiss, T.; Hartmann, P.; Zeier, W. G.; Janek, J., Interfacial Processes and Influence of Composite Cathode Microstructure Controlling the Performance of All-Solid-State Lithium Batteries. ACS Applied Materials & Interfaces 2017, 9 (21), 17835-17845.
- 15. Sakuda, A.; Hayashi, A.; Tatsumisago, M., Interfacial Observation between LiCoO₂ Electrode and Li₂S-P₂S₅ Solid Electrolytes of All-Solid-State Lithium Secondary Batteries Using Transmission Electron Microscopy. *Chemistry of Materials* **2010**, *22* (3), 949-956.
- 16. Park, K. H.; Oh, D. Y.; Choi, Y. E.; Nam, Y. J.; Han, L.; Kim, J.-Y.; Xin, H.; Lin, F.; Oh, S. M.; Jung, Y. S., Solution-Processable Glass Lil-Li₄SnS₄ Superionic Conductors for All-Solid-State Li-lon Batteries. *Advanced Materials* **2016**, *28* (9), 1874-1883.
- 17. Nagao, M.; Hayashi, A.; Tatsumisago, M., High-capacity Li₂S–nanocarbon composite electrode for all-solid-state rechargeable lithium batteries. *Journal of Materials Chemistry* **2012**, *22* (19), 10015-10020.
- 18. Chen, H.; Aalto, T.; Vanita, V.; Clemens, O., Effect of Uniaxial Stack Pressure on the Performance of Nanocrystalline Electrolytes and Electrode Composites for All-Solid-State Fluoride-Ion Batteries. *Small Structures* **2024**, *5* (7), 2300570.
- 19. Liu, W.; Luo, Y.; Hu, Y.; Chen, Z.; Wang, Q.; Chen, Y.; Iqbal, N.; Mitlin, D., Interrelation Between External Pressure, SEI Structure, and Electrodeposit Morphology in an Anode-Free Lithium Metal Battery. *Advanced Energy Materials* **2024**, *14* (5), 2302261.
- 20. Wei, C.; Liu, C.; Xiao, Y.; Li, Y.; Jiang, Z.; Liang, X.; Cao, K.; Cheng, S.; Huang, Y.; Yu, C., Pressure Tuning and Sn Particle Size Optimization for Enhanced Performance in PbSnF₄-Based All-Solid-State Fluoride Ion Batteries. *Small n/a* (n/a), 2401502.
- 21. Gao, X.; Liu, B.; Hu, B.; Ning, Z.; Jolly, D. S.; Zhang, S.; Perera, J.; Bu, J.; Liu, J.; Doerrer, C.; Darnbrough, E.; Armstrong, D.; Grant, P. S.; Bruce, P. G., Solid-state lithium battery cathodes operating at low pressures. *Joule* **2022**, *6* (3), 636-646.
- 22. Liu, B.; Pu, S. D.; Doerrer, C.; Spencer Jolly, D.; House, R. A.; Melvin, D. L. R.; Adamson, P.; Grant, P. S.; Gao, X.; Bruce, P. G., The effect of volume change and stack pressure on solid-state battery cathodes. *SusMat* **2023**, *3* (5), 721-728.
- 23. Lee, C.; Kim, J. Y.; Bae, K. Y.; Kim, T.; Jung, S.-J.; Son, S.; Lee, H.-W., Enhancing electrochemomechanics: How stack pressure regulation affects all-solid-state batteries. *Energy Storage Materials* **2024**, *66*, 103196.
- 24. Sakabe, J.; Ohta, N.; Ohnishi, T.; Mitsuishi, K.; Takada, K., Porous amorphous silicon film anodes for high-capacity and stable all-solid-state lithium batteries. *Communications Chemistry* **2018**, *1* (1), 24.
- 25. Tan, D. H. S.; Chen, Y.-T.; Yang, H.; Bao, W.; Sreenarayanan, B.; Doux, J.-M.; Li, W.; Lu, B.; Ham, S.-Y.; Sayahpour, B.; Scharf, J.; Wu, E. A.; Deysher, G.; Han, H. E.; Hah, H. J.; Jeong, H.; Lee, J. B.; Chen, Z.; Meng, Y. S., Carbon-free high-loading silicon anodes enabled by sulfide solid electrolytes. *Science* **2021**, *373* (6562), 1494-1499.
- 26. Lu, P.; Wu, Y.; Wu, D.; Song, F.; Ma, T.; Yan, W.; Zhu, X.; Guo, F.; Lu, J.; Peng, J.; Chen, L.; Li, H.; Wu, F., Rate-limiting mechanism of all-solid-state battery unravelled by low-temperature test-analysis flow. *Energy Storage Materials* **2024**, *67*, 103316.
- 27. Lu, Y.; Zhao, C.-Z.; Huang, J.-Q.; Zhang, Q., The timescale identification decoupling complicated kinetic processes in lithium batteries. *Joule* **2022**, *6* (6), 1172-1198.
- 28. Zhang, R.; Kondrakov, A.; Janek, J.; Brezesinski, T., Timescale Identification of Electrochemical Processes in All-Solid-State Batteries Using an Advanced Three-Electrode Cell Setup. *Energy Storage Materials* **2025**, 104000.
- 29. Li, L.; Fang, C.; Wei, W.; Zhang, L.; Ye, Z.; He, G.; Huang, Y., Nano-ordered structure regulation in delithiated Si anode triggered by homogeneous and stable Li-ion diffusion at the interface. *Nano Energy* **2020**, *72*, 104651.

- 30. Soni, R.; Robinson, J. B.; Shearing, P. R.; Brett, D. J. L.; Rettie, A. J. E.: Millery Tricle Online S., Lithium-sulfur battery diagnostics through distribution of relaxation times analysis. *Energy Storage Materials* **2022**, *51*, 97-107.
- 31. Mohammad, I.; Witter, R.; Fichtner, M.; Anji Reddy, M., Room-temperature, rechargeable solid-state fluoride-ion batteries. *ACS Applied Energy Materials* **2018**, *1* (9), 4766-4775.
- 32. Chen, H.; Schoch, R.; Chotard, J.-N.; Thiebes, Y. M.; Wissel, K.; Niewa, R.; Bauer, M.; Clemens, O., Revealing an Intercalation Nature of High-Capacity Conversion Cathode Materials for Fluoride-Ion Batteries by Operando Studies. *Small Methods n/a* (n/a), 2500374.
- 33. Perl, J.; Shin, J.; Schumann, J.; Faddegon, B.; Paganetti, H., TOPAS: an innovative proton Monte Carlo platform for research and clinical applications. *Med Phys* **2012**, *39* (11), 6818-37.
- 34. Croatto, U., Edifici cristallini con disordine reticolare. Fluoruro di piombo e bismuto. *Gazz. chim. ital.* **1944,** *74*, 20-20.
- 35. Aurivillius, B.; Brosset, C.; Ledaal, T.; Seip, H., The Crystal Structure of Bismuth Oxide Fluoride. *Acta Chem. Scand* **1964**, *18* (8), 1823-1830.
- 36. Cucka, P.; Barrett, C. S., The crystal structure of Bi and of solid solutions of Pb, Sn, Sb and Te in Bi. *Acta Crystallographica* **1962**, *15* (9), 865-872.
- 37. Greis, O. M.-R., M., Darstellung, Temperaturverhalten und Kristallstruktur von BiF₃. Zeitschrift für anorganische Chemie **1977**, *4*36.
- 38. Schneider, C.; Schmidt, C. P.; Neumann, A.; Clausnitzer, M.; Sadowski, M.; Harm, S.; Meier, C.; Danner, T.; Albe, K.; Latz, A.; Wall, W. A.; Lotsch, B. V., Effect of Particle Size and Pressure on the Transport Properties of the Fast Ion Conductor t-Li7SiPS8. *Advanced Energy Materials* **2023**, *13* (15), 2203873.
- 39. Lu, Y.; Huang, X.; Ruan, Y.; Wang, Q.; Kun, R.; Yang, J.; Wen, Z., An in situ element permeation constructed high endurance Li–LLZO interface at high current densities. *Journal of Materials Chemistry A* **2018**, *6* (39), 18853-18858.
- 40. Hassel, O.; Nilssen, S., Der Kristallbau des BiF₃. Zeitschrift für anorganische und allgemeine Chemie **1929**, *181* (1), 172-176.
- 41. Hund, F.; Fricke, R., Der Kristallbau von α-BiF₃. *Zeitschrift für anorganische Chemie* **1949**, *258* (3-5), 198-204.
- 42. Sorokin, N. I.; Karimov, D. N., Ionic Conductivity and Thermal Stability of BiF₃ Crystals. *KG* **2023**, *68* (2), 285-289.
- 43. Nagasaka, K.; Jinno, G.; Miura, O.; Miura, A.; Moriyoshi, C.; Kuroiwa, Y.; Mizuguchi, Y., Synchrotron powder X-ray diffraction and structural analysis of Eu_{0.5}La_{0.5}FBiS_{2-x}Se_x. *Journal of Physics: Conference Series* **2017**, *871* (1), 012007.
- 44. Christopoulos, S. R. G.; Kordatos, A.; Cooper, M. W. D.; Fitzpatrick, M. E.; Chroneos, A., Activation volumes of oxygen self-diffusion in fluorite structured oxides. *Materials Research Express* **2016**, *3* (10), 105504.
- 45. Park;, E. T. P. J.-H. In *Pressure Effecton Ionic Condaty in Yttrium-Oxide-Doped Single-Crystal Zirconium Oxide*, 3rd International Meeting of Pacific Rim Ceramic Societies, 1998.
- 46. Liu, J.; Zang, Z.; Yi, L.; Zeng, P.; Zou, C.; Chen, X.; Tao, X.; Yang, L.; Chang, B.; Shen, Y.; Wang, X., Constructing a BiF3/Bi7F11O5 multiple-phase composite as advanced cathode for room-temperature all-solid-state fluoride-ion batteries. *Journal of Electroanalytical Chemistry* **2023**, 928, 117073.
- 47. Ning, J.; Meng, W.; Wang, C.; Wang, H.; Wu, C.; You, L.; Wang, X.; Pei, Y.; Wang, H.; Yang, Z., Structure design of a BiOF solid electrolyte with remarkably outstanding fluoride ion diffusion performance induced by Ga doping. *Journal of Materials Chemistry A* **2024**, *12* (26), 15592-15600.
- 48. Sorokin, N. I.; Sobolev, B. P., Ionic conductivity of bismuth oxofluoride BiO_{0.1}F_{2.8} with tysonite-type structure (LaF₃). *Russian Journal of Electrochemistry* **2011**, *47* (1), 111-113.

Open Access Article. Published on 20 nuvembre 2025. Downloaded on 21/11/2025 21:53:44.

This article is licensed under a Creative Commons Attribution 3.0 Unported Licensed.

View Article Online DOI: 10.1039/D5TA06611E

Data availability statements

The data supporting this article have been included as part of the Supplementary Information

Crystallographic data for [o-BiF₃ *Pnma*] has been deposited at the [ICSD] under [1269] and can be obtained from [https://doi.org/10.1002/zaac.19774360112].

Crystallographic data for [c-BiF₃ *Fm*-3*m*] has been deposited at the [ICSD] under [24522] and can be obtained from [https://icsd.fiz-karlsruhe.de/display/details.xhtml].

Crystallographic data for [Bi] has been deposited at the [ICSD] under [64703] and can be obtained from [https://doi.org/10.1107/S0365110X62002297].

Crystallographic data for [BiOF] has been deposited at the [ICSD] under [24096] and can be obtained from [U https://icsd.fiz-karlsruhe.de/display/details.xhtml].

Crystallographic data for [BiF₃ *P*-3*c*] has been deposited at the [ICSD] under [29325] and can be obtained from [https://doi.org/10.1088/1742-6596/871/1/012007].

Crystallographic data for [BiO_{0.1}F_{2.8} *P4/nmm*] has been deposited at the [ICSD] under [24056] and can be obtained from [https://icsd.fiz-karlsruhe.de/display/details.xhtml].

Crystallographic data for [BaSnF₄ *P*4/*nmm*] has been deposited at the ICSD] under [166207] and can be obtained from [https://doi.org/10.1063/1.3234393].